Supramolecular bimetallic assemblies for photocatalytic hydrogen generation from water

Kowacs, Tanja; Pan, Qing; Lang, Philipp; O'Reilly, Laura; Rau, Sven; Browne, Wesley R; Pryce, Mary T; Huijser, Annemarie; Vos, Johannes G

IMPORTANT NOTE: You are advised to consult the publisher's version (publisher's PDF) if you wish to cite from it. Please check the document version below.

Document Version
Publisher's PDF, also known as Version of record

Link to publication in University of Groningen/UMCG research database

PAPER

Supramolecular bimetallic assemblies for photocatalytic hydrogen generation from water†

Tanja Kowacs,[a] Qing Pan,[b] Philipp Lang,[a] Laura O'Reilly,[c] Sven Rau,[a] Wesley R. Browne,*[d] Mary T. Pryce,[c] Annemarie Huijser*[b] and Johannes G. Vos*[c]

A series of supramolecular assemblies of the type $[Ru(L-L)_2(L'-L)MX_2)]^{n+}$ are reported where L-L is 2,2'-bipyridine (bipy), 4,4'-di-tetra-butyl-bipyridine (tbbipy) or 4,4'-diethoxycarbonyl-2,2'-bipyridine (dceb), L-L' is tetrapyrido[3,2-*a*:2',3'-*c*:3'',2''-*h*:2''',3'''-*j*]phenazine (tpphz), 2,2':5',2''-terpyridine (2,5-bpp), 2,2':6',2''-terpyridine, (2,6-bpp), 2,5-di(pyridine-2-yl)pyrazine (2,5-dpp) or 2,3-di(pyridine-2-yl)pyrazine (2,3-dpp), and MX_2 is $PdCl_2$, $PtCl_2$ or PtI_2. The photocatalytic behaviour with respect to hydrogen generation of these compounds and their ultrafast photophysical properties are discussed as a function of the nature of the peripheral ligands, the bridging ligands and the catalytic centre. The results obtained show how differences in the chemical composition of the photocatalysts can affect intramolecular photoinduced electron transfer processes and the overall photocatalytic efficiency.

Introduction

Recently, atmospheric CO_2 concentrations of 400 ppm were reported, the highest level for thousands of years. It is now widely accepted that atmospheric CO_2 levels have increased primarily due to anthropogenic activity, in particular due to the burning of fossil fuels. The effect that the increase in atmospheric CO_2 levels has on climate has spurred the development of alternative carbon-neutral energy strategies that enable continuation of the energy supply for a still growing global

[a]*Institut für Anorganische Chemie I, Universität Ulm, Albert-Einstein-Allee 11, 89081 Ulm, Germany*

[b]*Optical Sciences group, MESA+ Institute for Nanotechnology, University of Twente, P.O. Box 217, 7500 AE, Enschede, The Netherlands. E-mail: j.m.huijser@utwente.nl*

[c]*SRC for Solar Energy Conversion, School of Chemical Sciences, Dublin City University, Glasnevin, Dublin 9, Ireland. E-mail: han.vos@dcu.ie*

[d]*Stratingh Institute for Chemistry, Faculty of Mathematics and Natural Sciences, University of Groningen, Nijenborgh 4, 9747 AG, Groningen, The Netherlands. E-mail: w.r.browne@rug.nl*

population.[1,2] Such strategies need to be efficient, economically viable and above all carbon neutral in order to allow CO_2 levels in the atmosphere to reduce to pre-industrial revolution levels.

Over the last decades alternative energy sources including wind, photovoltaic, wave and tidal sources have seen rapid development with wind energy being most prominent. However, local opposition to the presence of wind turbines and the poor predictability of the variation of local wind strength creates challenges in terms of intermittent energy output; this latter aspect is faced by wave and tidal energy also. Solar driven devices are widely considered to be one of the more promising options for environmentally friendly energy. The Sun provides virtually unlimited energy and the global availability is *ca.* 4.93 MJ m^{-2} (1.37 kW h m^{-2}).[3] This translates into a usable energy of *circa* 3×10^{24} J per annum, more than 10 000 times the current annual global energy demand. Several approaches to harvesting solar energy with photovoltaic cells based on silicon or alternatively, dye sensitised solar cells as first developed by Grätzel and co-workers have made an already enormous impact.[4] However, photovoltaic cells produce electricity that must be used instantly and cannot be stored easily. An alternative and complementary approach is to develop molecular photocatalytic cells that instead of electricity produce fuels or chemical feedstocks from water or CO_2 by direct use of solar energy.[5]

In this contribution, we focus on the development of novel light driven molecular assemblies able to store solar energy through light induced generation of hydrogen from water. Supramolecular design principles utilised in the development of such molecular photocatalysts will be discussed with a particular focus on the relation between the ultrafast photophysical properties of these compounds and their efficiency towards photocatalytic hydrogen generation. Attempts to draw general conclusions regarding structure–activity relations will be highlighted.

The potential of molecular photocatalysts for hydrogen generation and CO_2 reduction has already been explored as early as the 1970s, in particular with intermolecular systems,[6] however, recently there has been increasing attention given to supramolecular photocatalysts. In both approaches a photosensitiser is
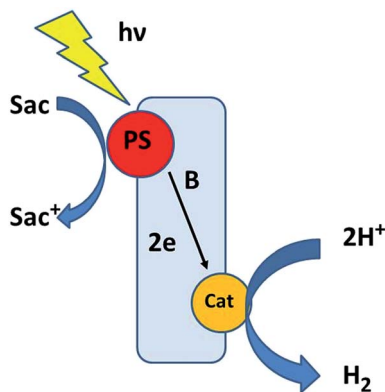

Fig. 1 Intramolecular approach. Sac = sacrificial reductant, PS = photosensitiser, Cat = catalytic centre, B = bridging ligand.

excited and electron transfer from the donor in the excited state to the catalytic centre occurs, either inter- or intramolecularly (Fig. 1). Sacrificial electron donors (S) such as triethylamine (TEA) are added to regenerate the reduced form of the photosensitiser.[7]

Results and discussion

Photocatalytic processes

The development of intramolecular photochemical molecular devices is inspired by natural photosynthesis, where chains of porphyrin and carotenoid derivatives are arranged precisely to optimise optical absorption and vectorial energy transfer to a photoredox active centre. Charge separation is achieved by directional electron transfer from the excited centre forming the basis for catalytic redox processes. The excited photocentre is quenched by an ultrafast photoinduced electron transfer to a primary acceptor (pheophytin) and further to a quinone leading to a long lived charge separated state. The radical cationic photocentre generated is reduced *via* an electron transfer chain with redox equivalents from the $CaMn_4$ oxygen evolving complex (OEC). Both the reduced quinone as well as the oxidised OEC are utilised in productive redox steps yielding $NADPH_2^+$ (nature's 'H$_2$') and O_2 from water, respectively. In synthetic systems a similar non-covalent supramolecular approach is beyond our reach, and the intramolecular option has therefore attracted the most attention with a wide range of hetero-oligometallic complexes with built in light harvesting and photocatalytic centres for hydrogen generation.[7–12]

Interest in heterooligometallic photocatalysts for the photogeneration of hydrogen arises from the potential of such assemblies to engage in *intra-* rather than *inter*-molecular electron transfer processes. This approach overcomes the ultimate limit on reaction rates (*i.e.* diffusion) and may lead to improved photocatalytic efficiency. One of the first examples of an intramolecular system that showed photocatalytic activity was $[(tbbipy)_2Ru(tpphz)PdCl_2](PF_6)_2$ (**1**), where tpphz = tetrapyrido[3,2-*a*:2′,3′-*c*:3′′,2′′-*h*:2′′′,3′′′-j]phenazine and tbbipy = 4,4′-di-tetra-butyl-bipyridine (Fig. 2).[13] With **1**, hydrogen can be generated in acetonitrile containing 10% water with a turnover number (TON) of 238 after 18 h with continuous wave irradiation at 470 nm, presumably *via* a mechanism such as that shown in Fig. 2.[14] In addition, a sacrificial agent, for example triethylamine (TEA), is necessary to regenerate the Ru(II) centre and allow the photocatalytic process to undergo further photocycles (Fig. 2).

It is quite evident from recent reports that spectroscopic methods are very well suited to elucidate the first light induced electron transfer steps.[7a,10a,c,11] However, the reduction with TEA already leads to significant changes in spectroscopic behaviour.[15] To date the essential second electron transfer step has been investigated spectroscopically for the related complex $[(tbbipy)_2Ru(tpphz)PtCl_2](PF_6)_2$. In this latter study, mimicking the conditions for hydrogen evolution, electrochemical reduction leads to the formation of a relatively long lived species with a radical anionic bridging ligand, however, further electron transfer along the bridging ligand was found to be impeded.[16] Note that in these experiments a proton donor was not present and hence stabilisation of such a negative charge by hydrogen bonding would be expected under catalytic conditions.
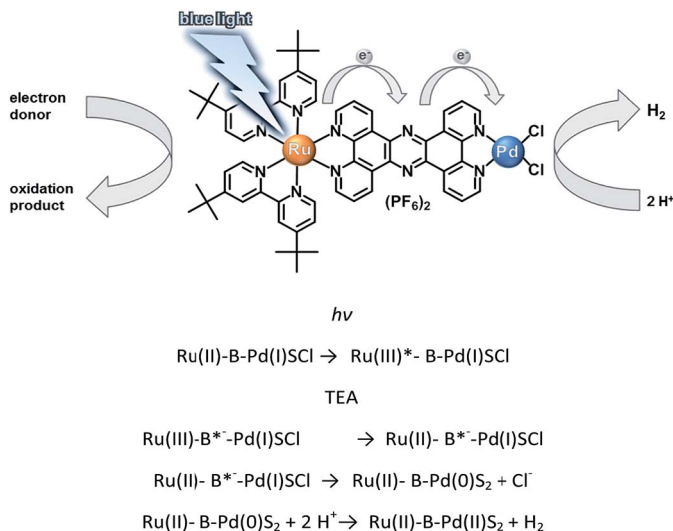
$$hv$$
$$\text{Ru(II)-B-Pd(I)SCl} \rightarrow \text{Ru(III)*- B-Pd(I)SCl}$$

$$\text{TEA}$$

$$\text{Ru(III)-B*}^-\text{-Pd(I)SCl} \qquad \rightarrow \text{Ru(II)- B*}^-\text{-Pd(I)SCl}$$

$$\text{Ru(II)- B*}^-\text{-Pd(I)SCl} \rightarrow \text{Ru(II)- B-Pd(0)S}_2 + \text{Cl}^-$$

$$\text{Ru(II)- B- Pd(0)S}_2 + 2\,\text{H}^+ \rightarrow \text{Ru(II)-B-Pd(II)S}_2 + \text{H}_2$$

Fig. 2 Basic mechanism of photocatalytic hydrogen production with **1** as photocatalyst. Light is absorbed by the Ru(II) moiety with subsequent electron transfer to the catalytic metal centre (Pd/Pt) mediated by tpphz. The sacrificial reductant is triethyl amine (TEA). B = bridging ligand, S = solvent.

The nature of the bridging ligand is an important issue also. Ishitani and co-workers have, in their studies of the photocatalytic reduction of CO_2, taken the approach that to avoid a fast back electron transfer, there should be only limited electronic coupling *via* the bridge.[17] Our group and others, focusing on the photocatalytic generation of hydrogen from water, have found that electronic coupling between the two reaction centres is important in achieving efficient hydrogen generation.[7] In the following discussion we will consider the effect of
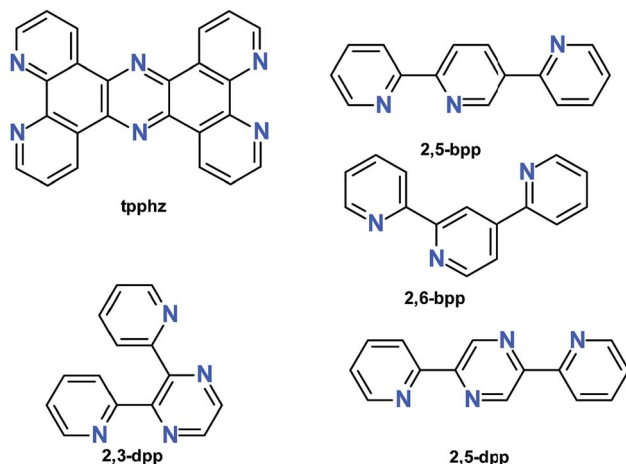

Fig. 3 Structures and abbreviations of bridging ligands discussed in the text.

1 = M = Pd, X = Cl
2 = M = Pt, X = Cl
3 = M = Pt, X = I

4

6 R = H
7 R = EtCOO

5

8 R = H
9 R = EtCOO

10 R = H;   X = Cl
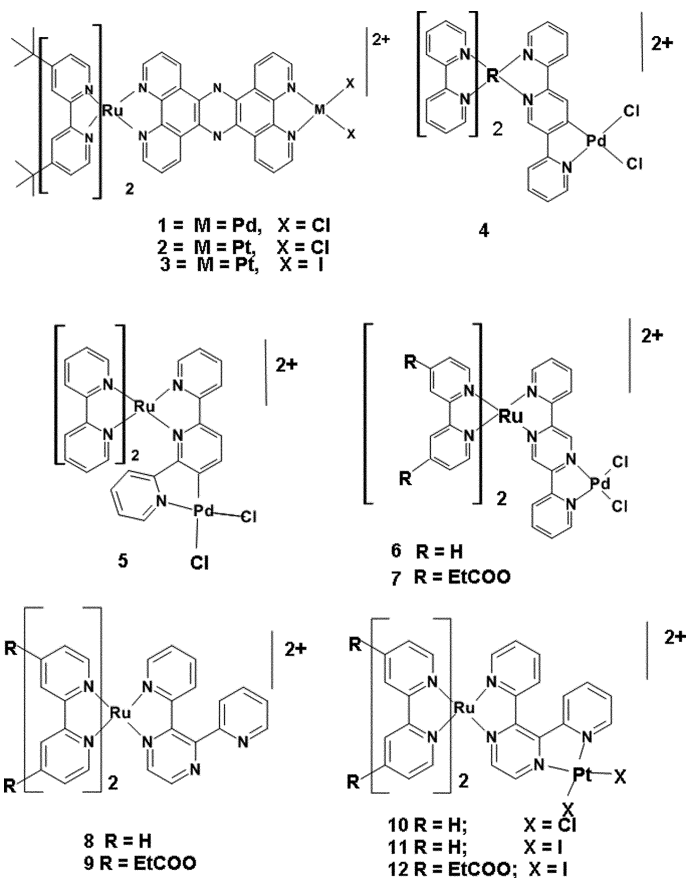11 R = H;   X = I
12 R = EtCOO; X = I

Fig. 4   Structures of complexes discussed in the text.

variation in the molecular components such as the nature of the bridging ligand, the peripheral ligands (Fig. 3) and the catalytic centre of the supramolecular assemblies (Fig. 4) on the photocatalytic behaviour observed.

The discussion is centred upon recent work concerning 1–7 and new data obtained for 8–12 (Fig. 4) and explores the relations between the photophysical properties of the various compounds and their photocatalytic behaviour as expressed in TONs and turnover frequencies (TOFs).

Assuming that the photoinduced interaction between the two reaction centres is important, the photophysical features of photocatalytic assemblies need to be designed carefully to allow for efficient photoinduced electron transfer from the photosensitiser to the catalytic centre. A typical, "first generation" scheme that facilitates vectorial photoelectron transfer from the photosensitiser to the catalytic centre is shown in Scheme 1.

Photophysical and photocatalytic studies

UV/vis absorption and emission spectral data for 1–12 together with their photocatalytic performance are summarised in Table 1.
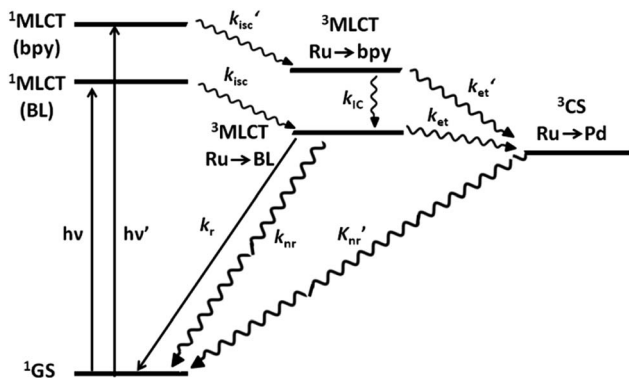
Scheme 1 Photoinduced pathways in supramolecular photocatalysts. BL = bridging ligand, CS = charge separated state.

In our recent studies on the design of supramolecular assemblies for light driven hydrogen generation, we have concentrated on the application of ruthenium polypyridyl photosensitisers and Pd or Pt based hydrogen evolving catalysts, bound to a common 'bridging' ligand (Fig. 3). Apart from the terpyridine type ligands, 2,5- and 2,6-bpp, these ligands incorporate the pyrazine motif, chosen to lower the $\pi*$ level of the bridging ligands, and thereby aiding vectorial electron

Table 1 Photophysical and photocatalytic properties of compounds discussed

Compounds	TON (18 h)	Abs λ_{max}/nm (log ε)	Emission λ_{max}/nm (τ/ns)[a]	Reference
[(tbbipy)$_2$Ru(tpphz) PdCl$_2$](PF$_6$)$_2$ (**1**)	238	445	652(27)	14
[(tbbipy)$_2$Ru(tpphz) PtCl$_2$](PF$_6$)$_2$ (**2**)	7(18)	442(17.60)	N/A	23
[(tbbipy)$_2$Ru(tpphz) PtI$_2$](PF$_6$)$_2$ (**3**)	279(70 h)	437(19.70)	N/A	24
[Ru(bipy)$_2$(2,5-bpp)PdCl$_2$]$^{2+}$ (**4**)	138	463(4.12)	635(105)	18
[Ru(bipy)$_2$(2,6-bpp)PdCl$_2$]$^{2+}$ (**5**)	0	449	635(>1)	18
[Ru(bipy)$_2$(2,5-dpp)PdCl$_2$]$^{2+}$ (**6**)	0	539(4.00)	807(>0.5)	19
[Ru(dceb)$_2$(2,5-dpp)PdCl$_2$]$^{2+}$ (**7**)	400	526(4.20)	778(>0.5)	19
[Ru(bipy)$_2$(2,3-dpp)]$^{2+}$ (**8**)	N/A	441(3.96)	645(373)	This work
[Ru(dceb)$_2$(2,3-dpp)]$^{2+}$ (**9**)	N/A	463(1.63)	635(1075)	This work
[Ru(bipy)$_2$(2,3-dpp)PtCl$_2$]$^{2+}$ (**10**)	0	516(4.27)	773(vw)	20 & this work
[Ru(bipy)$_2$(2,3-dpp)PtI$_2$]$^{2+}$ (**11**)	0	516(4.32)	778(vw)	This work
[Ru(dceb)$_2$(2,3-dpp)PtI$_2$]$^{2+}$ (**12**)	44	485(4.25)	—	This work

[a] Argon purged. The photocatalytic TONs were determined in a mixture of acetonitrile/water (10%) with the sacrificial agent TEA under N$_2$.

transfer from the photosensitiser to the catalytic centre. It is apparent (Table 1) that a simple relation between the nature of the bridging ligand and efficiency in terms of photocatalytic performance (*i.e.* TON) is absent. For the tpphz based compounds **1–3** the TONs show a dependence on the nature of the catalytic centre, while for the terpyridine based compounds only **4**, which contains the linear 2,5-bpp bridge, is catalytically active. Furthermore for the 2,3- and 2,5-dpp bridged compounds, only those bearing Ru(dceb)$_2$ moieties, *i.e.* **7** and **12**, are catalytically active. These latter observations, surprisingly, indicate that in addition to the bridging ligand, the nature of the peripheral ligands and the catalytic centre need to be considered also.

Indeed, the earlier reports by Rau and co-workers[13] indicated that the peripheral ligands play an important role, with TONs for **1** dependent on the wavelength of excitation between 400 and 530 nm. Catalytic activity was greatest at *ca.* 500 nm despite the relatively low molar absorptivity at this wavelength. It is important to note however that the absorption band at 500 nm for **1**, is predominantly a metal to bridging ligand charge transfer transition. Thus, the catalytic activity of **1** does not strictly follow the absorption spectrum, and irradiation directly into absorption bands involving the peripheral ligands reduces the efficiency of hydrogen formation.

A wavelength dependence of the catalytic activity has been observed for Ir(III) compounds also, and in those cases it was proposed that direct excitation into rather weak triplet metal-to-ligand charge-transfer (^{3}MLCT) excited states is more efficient towards photocatalytic generation of hydrogen than excitation into intraligand charge transfer (ILCT) states.[21] These data indicate that excitation into states involving primarily the peripheral ligands does not necessarily result in internal conversion to excited states involving the bridging ligand, *i.e.* that the electronic coupling between excited states localised on peripheral and bridging ligands is not necessarily strong. These conclusions raise two questions: how efficient is internal conversion between excited states involving the peripheral ligands to those involving the bridging ligand, and can the photocatalytic efficiency be controlled by the choice of ligands and/or irradiation wavelength. Furthermore these observations have prompted a reconsideration of the "first generation" photophysical model (Scheme 1).

Recently, our groups have focused on the fs–ps photophysics of **1** to gain a deeper understanding of the photocatalytic properties of supramolecular photocatalysts.[22] Steady state (CW), ns-time resolved resonance Raman (nsTR^3) and fs-transient absorption (TA) spectroscopies have been applied to elucidate the photophysical properties of these photocatalysts in CH$_3$CN under non-catalytic conditions, *i.e.* in the absence of sacrificial reductant and water. Carrying out similar studies in the presence of the sacrificial agents has thus far proven highly challenging due to the interference of the oxidation products. An overview of the excited state dynamics indicates directional electron transfer occurs in both **1** and its precursor **1a** (Scheme 2).

In both compounds the singlet metal-to-ligand charge-transfer excited states (^{1}MLCT) populated initially are based on the tbbipy and on the phenanthroline part of the tpphz bridging ligand, with relaxation to a ^{3}MLCT state manifold occurring on the fs-timescale. Relaxation to the triplet manifold is complete within 1.2 ps for **1a** and 0.8 ps for **1**. Considerable differences are observed, however, in the subsequent decay of this triplet excited state over 240 ps for **1a** to
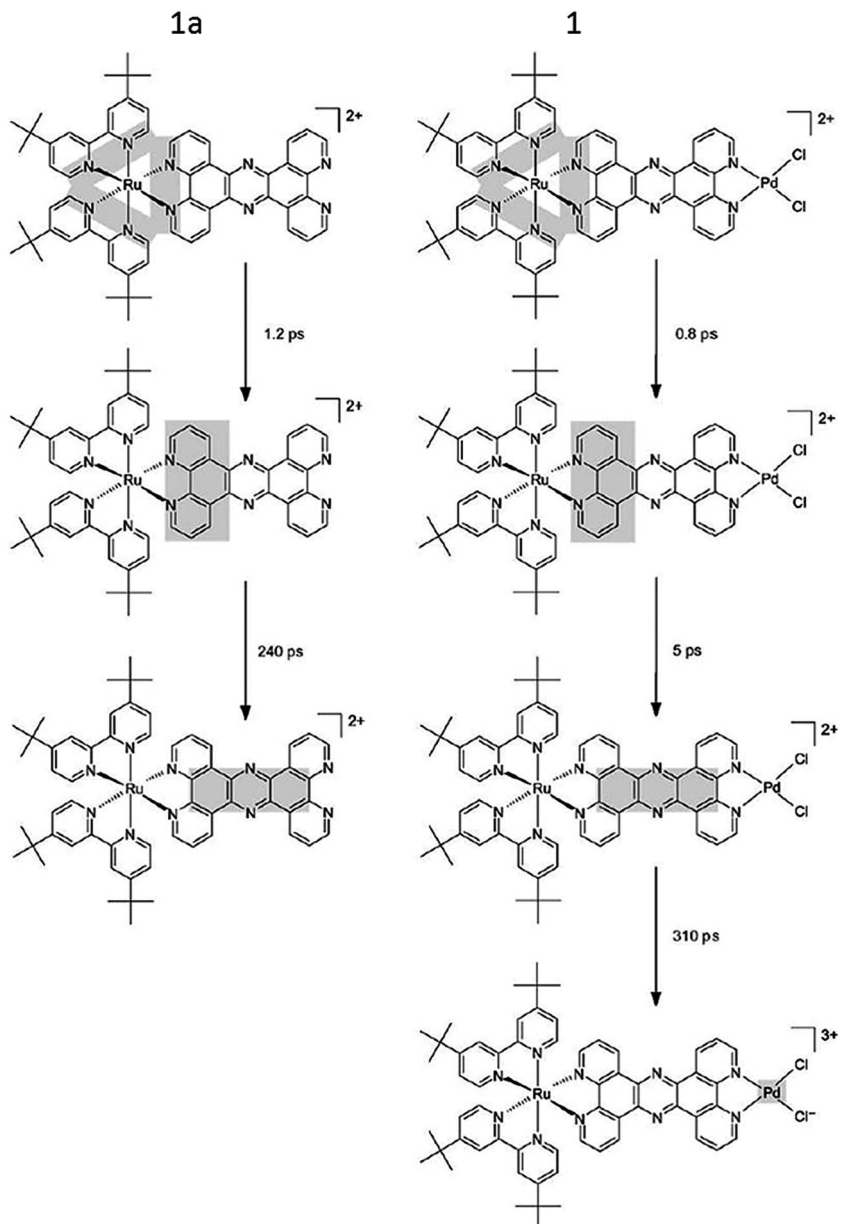
Scheme 2 Electron transfer dynamics of **1** and its precursor complex **1a**. Localisation of the electron in the photoexcited state is illustrated by shaded areas. Reproduced with permission from ref. 22.

an ILCT state localised on the phenazine unit, while for **1** this process is complete within 5 ps. The presence of the excited electron on the phenazine part of the bridging ligand was confirmed by electron paramagnetic resonance spectroscopy. These observations indicate that the presence of the Pd(II) centre significantly influences the electronic structure of the bridging ligand. For **1**, subsequent

Paper

population of a long-lived ligand to metal charge transfer (LMCT) state on the Pd(II) centre with a time constant of 310 ps was observed. The decay of this state was not observed since its timescale is greater than the instrumental range (*i.e.* >5 ns). In addition, it is important to note that while for **1a** emission is observed at 650 nm with a lifetime of 240 ns, for **1** a relatively weak emission at the same wavelength with a lifetime of <20 ns is observed, showing that the photophysics of **1a** are modified substantially by the introduction of the Pd(II) centre (*i.e.* **1**). Ultimately the reduction of the Pd(II) centre is expected to be accompanied by dissociation of a chloride anion.[13]

Analogues of this compound, where the $PdCl_2$ catalytic centre was replaced by a $PtCl_2$ (**2**) or a PtI_2 centre (**3**) were investigated also. Compound **2** showed a rather low TON of 7 but substantially increased chemical stability under catalytic conditions, *i.e.* platinum colloids were not formed.[23] Based on the results of the X-ray absorption data for **2** an optimised catalyst, **3**, in which iodide ligands increase the electron density at the platinum centre, was designed. It showed a 40 times higher TON of 279 associated with increased stability compared to **1**.[24] Importantly, the photophysical behaviour of the Pt analogues is similar to that discussed above for **1**. After excitation into the Franck–Condon states, fast intersystem crossing to the triplet manifold is observed with a time constant of less than 100 fs. Subsequently, population of an interligand electron transfer (ILET) state is observed (0.5 ps), followed by thermal equilibration to a ^{3}MLCT(phen) state within 2 ps. Subsequent population of an MLCT state, centred on the phenazine (phz) part of the bridging ligand (4 ps) is observed. Finally a 340 ps time constant is observed, which manifests the formation of a long-lived species as observed for **1**. The latter process is assigned to electron transfer to the PtI_2 moiety. These photoinduced processes are both qualitatively and quantitatively unaffected by the exchange of the $PtCl_2$ for a PtI_2 moiety.[23]

The results discussed above show that the exchange of the halide ligands of the catalytic platinum centre does not significantly change the intramolecular photophysics of the photocatalyst. However, both **2** and **3** do not show the induction period observed with **1**,[24] and the TOF is constant during catalysis. It is notable that whereas in **1** loss of a halide anion from the catalytic centre is necessary for it to engage in hydrogen formation, this is not the case for the Pt based catalysts. The replacement of $PtCl_2$ with PtI_2, however, leads to a substantial increase of photocatalytic activity, which is consistent with reports by Sakai and co-workers, who highlighted the importance of occupation of the d_z^2 orbital of the Pt centre for the generation of Pt–H intermediates.[20] The introduction of iodo ligands increases the electron density at the Pt centre and therefore is expected to stabilise such Pt–H intermediates, resulting in increased TONs for hydrogen generation. For **1**, directional electron transfer *via* the ^{1}MLCT states localised on the bridging or the peripheral ligands dictates the photocatalytic activity, as manifested in the wavelength dependence of the photocatalytic efficiency and wavelength dependent resonance Raman studies.[15] However, recent studies using the chemically more robust complex **2**, in which the photochemical properties of the electrochemically reduced **2**, where the charge is localized on the tpphz based phenazine orbital, indicate that the second photoinduced electron transfer *via* the already reduced bridging ligand is hindered.[16] However, the formation of H_2 requires addition of protons as well as the transfer of two electrons to the catalytic center – which is not possible in the spectroelectrochemical studies. The presence of

protons in solution may serve to reduce the barrier to electron transfer by hydrogen bonding with the phenazine nitrogens.

It is apparent (Table 1) that extensive and detailed photophysical studies of supramolecular assemblies are central to improving hydrogen generation capacity. In the following section the photophysical and photocatalytic properties of a number of the related compounds, **4** and **10–12**, will be discussed. Following on from the results obtained for the tpphz based compounds, the discussion will concentrate on the early photoinduced processes involving the peripheral and bridging ligands. The photophysical studies of **4** (ref. 18) and **10–12** were carried out in acetonitrile over the femto- to the submicro-second time domains.[25] In addition resonance Raman (rR) data are presented.

Resonance Raman spectroscopy has been shown to be a powerful tool to study the wave packet motion in the Franck–Condon region. Hence, identification of vibrational modes with strong resonance enhancement provides information about the orbital parentage (*i.e.* localisation) of the Franck–Condon states. This information is complementary to the photophysical studies such as transient absorption (TA) spectroscopy, which has a time resolution of 100–150 fs. Resonance Raman spectra of **4**, its precursor $[Ru(bipy)_2(2,5bpp)]^{2+}$ (**4a**) and $[Ru(bipy)_3]^{2+}$ recorded in acetonitrile are shown in Fig. 5. Band assignments were reported earlier.[25] At λ_{exc} 473 nm, which is close to the pump wavelength (480 nm) used in the TA experiments, the Raman scattering from the ligands associated with the ^{1}MLCT ← GS (GS: ground state) transitions is resonantly enhanced. In all three spectra, the characteristic modes of $[Ru(bipy)_3]^{2+}$ are observed and indicate resonance with ^{1}MLCT(t$_2$-Ru(II) to π*-bipy) transitions at 473 nm. Resonance with ^{1}MLCT(t$_2$-Ru(II) to π*-2,5-bpp) transition is observed for the precursor also, in particular the bands at 1606, ~1507, ~1473 and 1318 cm^{-1}. In the case of **4**, additional bands associated with the 2,5-bpp ligand are observed,
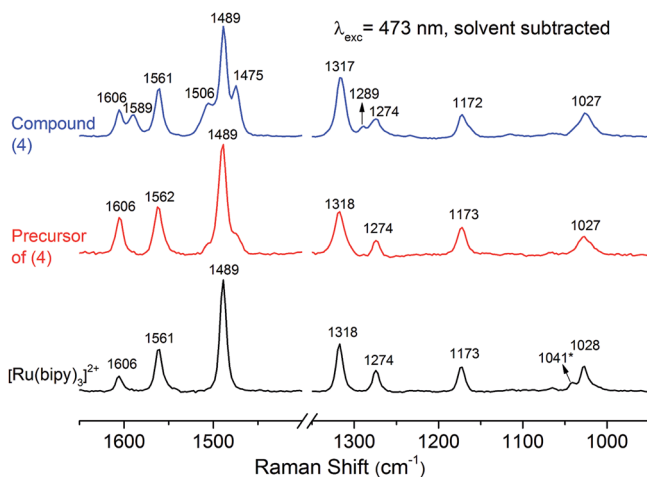

Fig. 5 Resonance Raman spectra of the precursor of 4 (*i.e.* **4a**) (red), **4** (blue) and $[Ru(bipy)_3]^{2+}$ (black) in acetonitrile (*ca.* 0.1 mM, solvent contributions have been removed by scaled subtraction) recorded at λ_{exc} 473 nm. Reproduced with permission from ref. 25. The band at 1041 cm^{-1} (*) is due to imperfect subtraction of the solvent signal.

e.g., at 1589 cm^{-1}, due to changes in ligand structure brought about by coordination of Pd(II). Note that some 2,5-bpp and bipy associated modes overlap at 1606 and 1318 cm^{-1}. In conclusion, resonance Raman confirms the initial population of both bipy and bridging ligand based ^{1}MLCT states in both **4a** and **4** upon excitation at 473 nm.

Assuming that the photophysical model shown in Scheme 1 holds for **4**, excitation should lead to the population of ^{1}MLCT states followed by efficient intersystem crossing (50–100 fs) from both the bipy and 2,5-bpp bridge based ^{1}MCLT states to a ^{3}MLCT state localised on the bridging ligand.[26–28] The veracity of this model was tested through time resolved absorption spectroscopy (TA) in the femto–picosecond timescale[25] on both **4a** and **4**. The intersystem crossing (ISC) processes are too fast to be studied by the experimental facilities available. The transient absorption spectra at various time delays between pump and probe are shown in Fig. 6.

In the spectra obtained for both compounds, an increase of the differential absorbance at >500 nm is observed, which is associated with a triplet ligand to metal charge transfer (^{3}LMCT) transition. A ground state bleach is observed
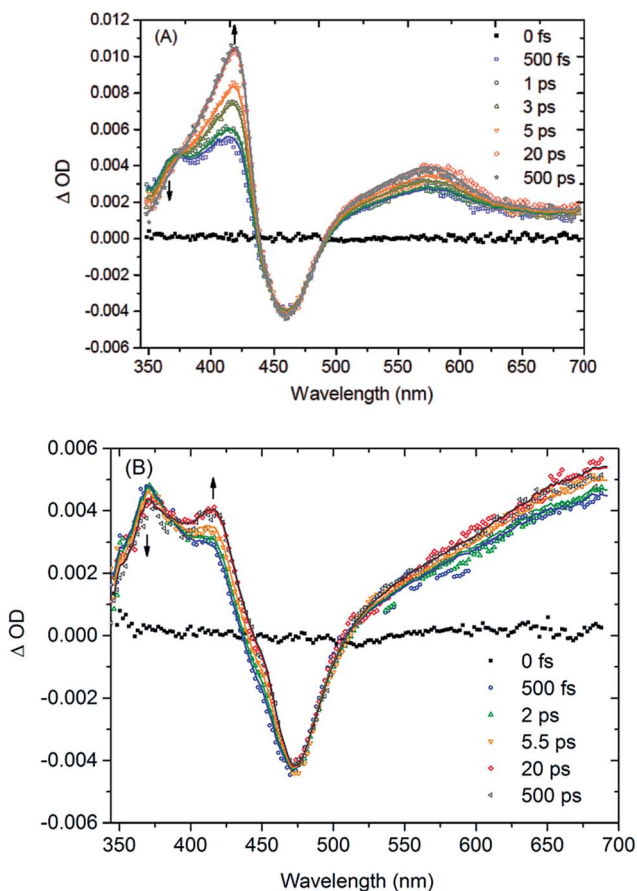

Fig. 6 Time resolved transition absorption spectra of the precursor (A) **4a** and (B) **4**. Adapted from ref. 25.

around 450 nm, as expected. The most informative region of the TA-spectra is 350–420 nm due to the anion radical based transitions (^{3}IL) present there. In this section this region will be discussed in more detail, since the changes observed manifest the population of ^{3}MLCT states based on the bridging and peripheral ligands. Two absorption bands are observed for **4a** (Fig. 6A), one at 370 nm, assigned to the bipy anion radical (*i.e.* a peripheral ligand based ^{3}MLCT state)[29] and at 420 nm associated with a state based on the 2,5-bpp ligand.[30] Notably a *decrease* in the absorbance at 370 nm occurs concomitantly with an *increase* of the 420 nm band, indicating internal conversion between a ^{3}MLCT$_{bipy}$ excited state to a ^{3}MLCT$_{2,5\text{-}bpp}$ excited state, (in other words, internal conversion from the peripheral to the bridging ligand), or alternatively equilibration of these states. In the latter case, electron transfer continues to take place in both directions. For **4** similar dynamics are observed with some minor differences related to the presence of the Pd(II) centre. Importantly, as observed for **4a** (Fig. 5A), the TA spectrum observed for **4** remains unchanged between 20 and 500 ps. These data indicate that electron transfer/delocalisation involving the bipy and 2,5-bpp ligands is complete within 20 ps.

4a and **4** show similar emission spectra, but with significantly different emission decay lifetimes. For **4a** a mono-exponential decay was observed with a lifetime of 623 ns suggesting that both ^{3}MLCT$_{bipy}$ and ^{3}MLCT$_{bpp}$ states decay at the same rate (*i.e.* equilibration). However, for **4** a biexponential decay was observed, with an 88 ns component (60%), assigned to emission from the ^{3}MLCT$_{2,5\text{-}bpp}$ state. The shorter emission lifetime is most likely related to enhanced spin–orbit coupling due to the Pd(II) centre. The second component (40%) with a lifetime of 400 ns is assigned to the decay from the bipy based triplet states. This interpretation implies that the bipy and 2,5-bpp based excited states are not equilibrating at these time scales, however. Based on these observations a photophysical model for the excited state behaviour can be proposed (Scheme 3).

The data indicate that optical excitation of **4** does not lead to population of only a bridging ligand based excited state. After excitation into the ^{1}MLCT states based on each of the ligands, only 21% (Scheme 3 and Fig. 5, *vide infra*)[31] is
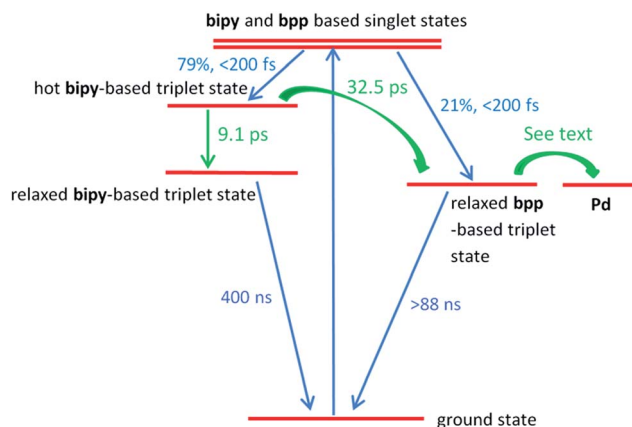
Scheme 3   Photophysical model for **4**. Adapted from ref. 25.

converted *via* ultrafast intersystem crossing into a ^{3}MLCT state localised on the bridging 2,5-bpp ligand; the majority of excitation leads to ^{3}MLCT states localised on the peripheral bipy ligands. The degree of population of the bipy and 2,5-bpp based ^{3}MLCT states was determined by inspecting the shape and position of the species associated spectra obtained by target analysis of the transient absorption data.[25] The intersystem crossing into the ^{3}MLCT states is followed by internal conversion (from the hot ^{3}MLCT$_{bipy}$ towards the ^{3}MLCT$_{bpp}$ state) which competes with vibrational cooling of the hot ^{3}MLCT$_{bipy}$ state (Scheme 3). The time-resolved emission data suggest that the electron transfer rate k_{et} from the bridging ligand to the Pd centre is of the order of 10^7 s^{-1}, although the possibility of a delocalized bpp-Pd state formed well before ~100 ns after excitation cannot be excluded. The presence of two distinct emission lifetimes suggests a weak interaction between the peripheral and bridging ligands. In the strong interaction case shown in Scheme 2 an almost complete quenching of the emission is expected, and this is observed for **1**.[13] The biexponential emission of **4** is surprising considering the proximity of the light absorbing Ru(II) moiety and the Pd(II) centre. The reason for this limited electronic coupling is at present not understood, but may be associated with the cyclometallation of the bridging ligand and delocalisation of the excited state over both the bridging ligand and the Pd(II) centre.

Photophysical properties of 8 and 10–12

In the following section the photocatalytic assemblies **10–12**, based on the 2,3-dpp bridging ligand, are discussed (Fig. 3 and 4). This ligand is not linear and in earlier studies by Sakai and co-workers[20] **10** did not display photocatalytic hydrogen generation. However, we show here that, as shown in Table 1, **12** can catalyse photoinduced hydrogen generation and this shows the strong effect that the introduction of an ester moiety can have on the catalytic process. The photophysical properties and resonance Raman spectroscopy of the complexes are considered and discussed with relevance to their photocatalytic properties.

    Absorption and emission spectroscopy of 8–12. Steady state UV/vis absorption and emission data are listed in Table 1. The UV/vis absorption spectrum of **8** shows (Fig. 7) a broad absorption with a λ_{max} 441 nm, in agreement with the literature.[20,32]

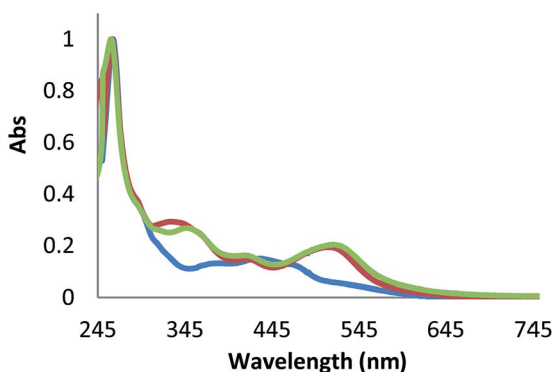Fig. 7 Absorption spectra (normalised) of [Ru(bpy)$_2$(2,3-dpp)]$^{2+}$ (**8**) (blue), [Ru(bpy)$_2$(2,3-dpp)PtCl$_2$]$^{2+}$ (**10**) (red) and [Ru(bpy)$_2$(2,3-dpp)PtI$_2$]$^{2+}$ (**11**) (green) at RT in acetonitrile.

The visible absorptions of the dinuclear Ru/Pt complexes **10** and **11**, are distinct from **8**, with two absorption bands at 419 nm and 516 nm (Fig. 7) and are similar to the absorption spectra of the dinuclear ruthenium complex [(bpy)$_2$-Ru(μ-2,3-dpp)Ru(bpy)$_2$]$^{4+}$,[33] consistent with lowering of the energy of the pyrazine based ^{1}MLCT states. The spectra of the iodo and chloro complexes are similar indicating relatively little influence of the PtX$_2$ unit on the lowest ^{1}MLCT states beyond stabilisation of the pyrazine based states. [Ru(bpy)$_2$(2,3-dpp)PtI$_2$]$^{2+}$ (**11**) shows a minor red shift of the shoulder of the $\pi \rightarrow \pi^*$ absorption bands and the Ru $\rightarrow$ 2,3-dpp transition is slightly stronger for the chlorido complex (see Table 1). The broadened absorption band in the UV region (shoulder between 300 and 360 nm) is assigned to ligand centred $\pi \rightarrow \pi^*$ transitions of the bridging ligand.

For **8**, an emission is observed at room temperature with a maximum at 645 nm. The dinuclear complexes show a large decrease in emission intensity and a shift in λ_{max} to 773 nm for **10** and 778 nm for **11**, consistent with double coordination of metal ions to the pyrazine moiety.[34]

9 shows a broad absorption with a maximum at 463 nm and a shoulder at 432 nm (Fig. 8). The absorption at 463 nm is red-shifted by about 20 nm compared to **8**. The absorption spectrum of **12** shows broad absorption bands between 440 to 520 nm with a maximum in the UV at *ca.* 350 nm assigned to LC transitions of the 2,3-dpp ligand and possibly also Pt $\rightarrow$ 2,3-dpp ^{1}MLCT transitions. **9** displays stronger emission than **8**, with a maximum at 635 nm. For **12** the emission is quenched (Table 1).

Resonance Raman spectroscopy. Ground state rR spectra were recorded for complexes **8–12** at λ_{exc} 355 nm, 457 nm and 473 nm with assignments added by comparison to the spectra of [Ru(bipy)$_3$]$^{2+}$. **8** shows resonantly enhanced bands at λ_{exc} 473 nm at 1029, 1173, 1274, 1318, 1489, 1561 and 1606 cm^{-1}, which are observed in the spectrum of [Ru(bipy)$_3$]$^{2+}$ also,[35] and indicate a ^{1}MLCT (Ru(II) $\rightarrow$ π^*-bipy) transition. Additional modes are apparent at 1064, 1247, 1265, 1302, 1404, 1426, 1453, 1471, 1520 and 1561 cm^{-1}, which are associated with a ^{1}MLCT (Ru(II) $\rightarrow$ π^*-2,3-dpp) transition. Hence, excitation at 473 nm leads to the initial
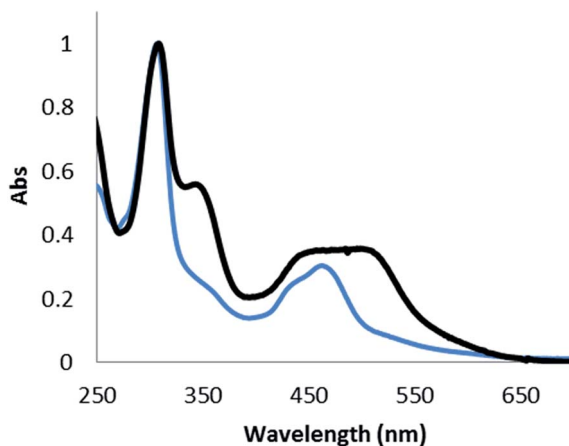

Fig. 8 Absorption spectra (normalised) and emission spectra of [Ru(dceb)$_2$(2,3-dpp)]$^{2+}$ (**9**) (blue) and [Ru(dceb)$_2$(2,3-dpp)PtI$_2$]$^{2+}$ (**12**) (black) at RT in acetonitrile.

population of both bipy and 2,3-dpp based ^{1}MLCT states. At λ_{exc} 457 nm population of both ^{1}MLCT states is also indicated, with a greater contribution from the bipy bands compared to the 2,3-dpp bands compared with excitation at 473 nm (see ESI, Fig. S9†).

The dinuclear complexes **10** and **11** (Fig. 9) show considerable overlap of the Raman bands from both the bipy and 2,3-dpp ligands with bands at 1029, 1068, 1182, 1247, 1265, 1318/1314, 1398/1401, 1471, 1489, 1497, 1561, 1575 and 1598 cm^{-1}. For **11**, two additional bands are observed at 1170 and 1519 cm^{-1}. The bands at 1489 and 1561 cm^{-1} are due to the bipy ligands, however, their relative intensity indicates that bands from the 2,3-dpp ligand are present at these wavenumbers also. Overall, it is apparent that the majority of the observed bands are associated with ^{1}MLCT (t_2-Ru(II) $\rightarrow$ π*2,3-dpp) transitions. Hence for **10** and **11**, rR spectroscopy indicates that mainly ^{1}MLCT states based on the bridging ligand are populated initially upon excitation at 473 nm.

At λ_{exc} 457 nm, the band at 1489 cm^{-1}, assigned tentatively as a bipy mode, is enhanced to a greater extent than at 473 nm, while at λ_{exc} 355 nm population of both bipy and 2,3-dpp based excited states is apparent (see ESI, Fig. S10†).

The rR spectra at λ_{exc} 473 nm of [Ru(dceb)$_2$(2,3-dpp)]$^{2+}$ (**9**) and [Ru(dceb)$_2$(2,3-dpp)PtI$_2$]$^{2+}$ (**12**) (Fig. 10) both show bands at 1027, 1256, 1270, 1322, 1478, 1554 and 1619 cm^{-1} with similar relative intensities, which are assigned to modes of the dceb ligands. The strong emission from **9** reduces substantially the S/N ratio of its rR spectrum at λ_{exc} 473 nm and precluded the recording of useful spectra at other wavelengths. Nevertheless, in addition to bands typical of dceb, excitation into a ^{1}MLCT(t_2-Ru(II) to π*-2,3-dpp) also is apparent from the weak band at 1522
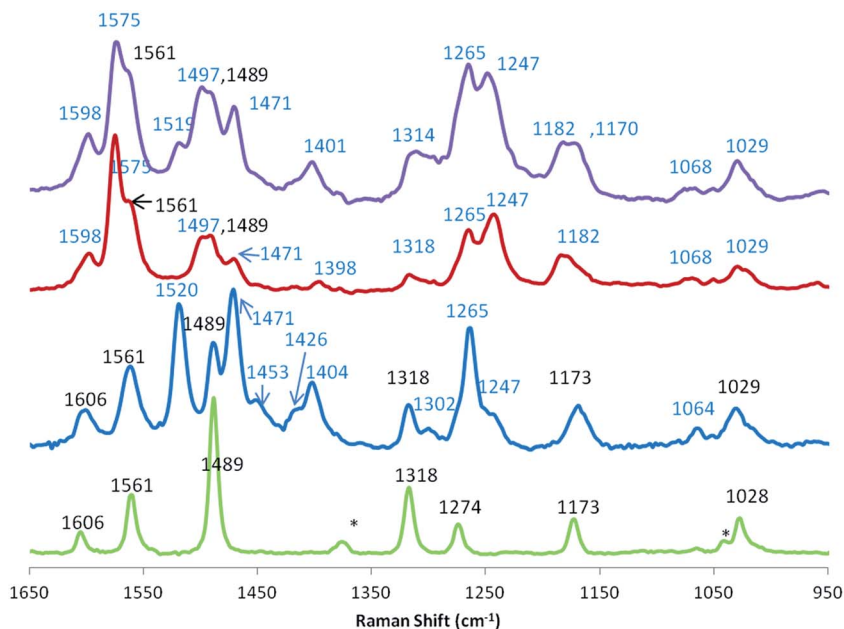
Fig. 9 The rR spectra at λ_{exc} 473 nm (normalised) of [Ru(bipy)$_3$]$^{2+}$ (green), [Ru(bpy)$_2$(2,3-dpp)]$^{2+}$ (**8**) (blue), [Ru(bpy)$_2$(2,3-dpp)PtCl$_2$]$^{2+}$ (**10**) (red) and [Ru(bpy)$_2$(2,3-dpp)PtI$_2$]$^{2+}$ (**11**) (purple) in acetonitrile. Bipy bands are indicated in black and 2,3-dpp bands in blue.

Fig. 10 The rR spectra at λ_{exc} 473 nm (normalised) of $[Ru(dceb)_2(2,3\text{-}dpp)]^{2+}$ (**9**) (blue) and $[Ru(dceb)_2(2,3\text{-}dpp)PtI_2]^{2+}$ (**12**) (purple) in acetonitrile. Bipy bands are indicated in black and 2,3-dpp bands in blue.
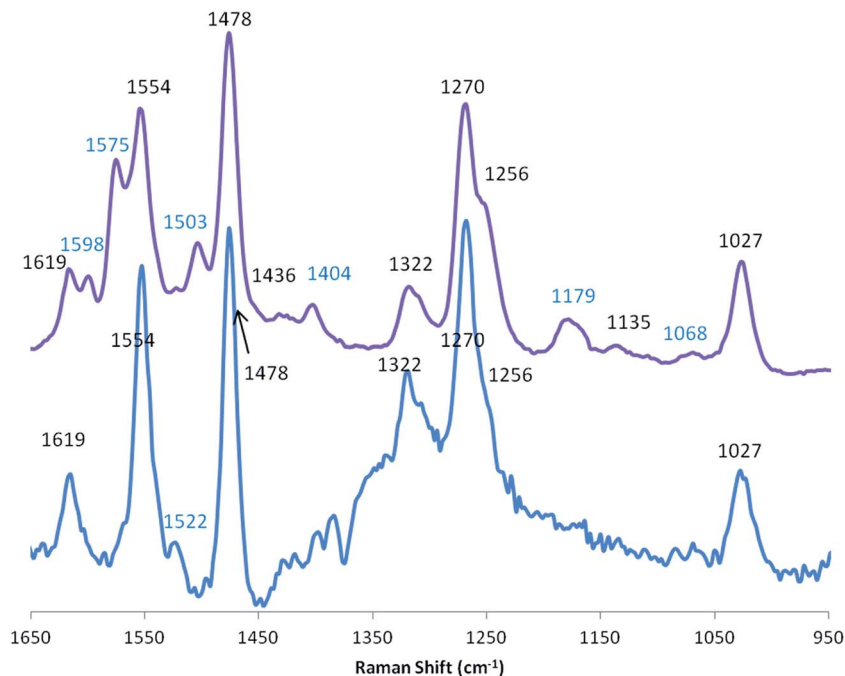
cm^{-1}, which is a resonantly enhanced 2,3-dpp mode. Hence rR spectroscopy indicates that mainly dceb based ^{1}MLCT states are initially populated upon excitation at 473 nm.

For **12**, upon excitation additional bands are observed that are assigned to the bridging 2,3-dpp ligand having intensities relative to the bipy bands that indicate better resonance with dceb based ^{1}MLCT ← GS transitions at this wavelength than observed for **10** and **11** (*vide supra*). These extra bands appear at 1068, 1179, 1404, 1503, 1575 and 1598 cm^{-1} arising from resonance with a ^{1}MLCT(t_2-Ru(II) to π*-2,3-dpp) transition. Therefore upon excitation of **12** at 473 nm both dceb and bridging ligand based ^{1}MLCT states are initially populated. rR spectra of **12** (Fig. 11) obtained at λ_{exc} 355 nm, 457 nm and 473 nm) show bands due to resonance with a 2,3-dpp based transition as well as dceb based transitions, with their relative intensity differing significantly over the three wavelengths. At λ_{exc} 473 nm, the bands of 2,3-dpp are enhanced to a greater extent relative to dceb than at λ_{exc} 457 nm, and at λ_{exc} 355 nm 2,3-dpp bands dominate the rR spectrum due to excitation into an intraligand transition. These data indicate that the gap between ^{1}MLCT states localised on the bridging 2,3-dpp ligand and the peripheral ligands is less in the case of dceb based complexes than for bipy based complexes.

The rR spectra for **8–12** present a clear picture of the nature of the Franck–Condon states. For **8**, excitation leads to population of both the bipy and the 2,3-dpp based excited states, while for **10** and **11**, excitation is predominantly into 2,3-dpp based excited states at 473 nm. Hence, binding of the Pt(II) centre lowers the
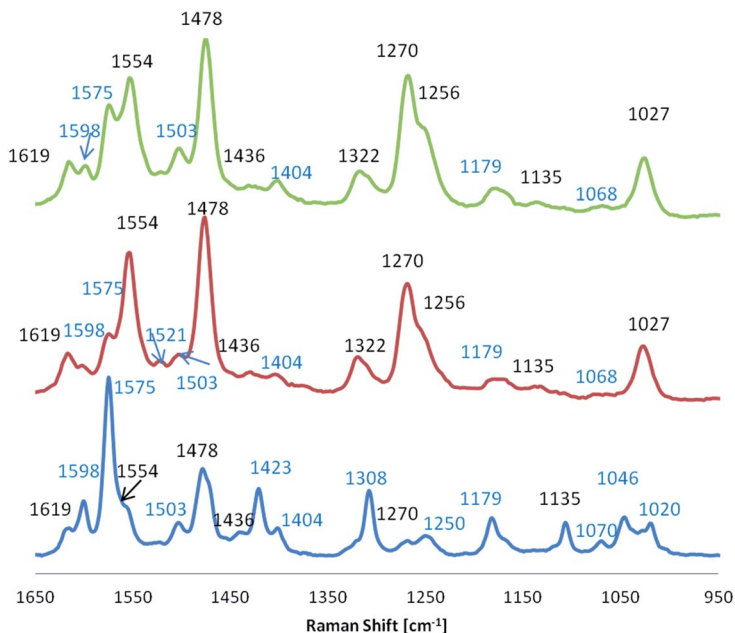
Fig. 11 The rR spectra (normalised) of $[Ru(dceb)_2(2,3\text{-}dpp)PtI_2]^{2+}$ (**12**) at λ_{exc} 355 nm (blue), 457 nm (red) and 473 nm (green) in acetonitrile. Bipy bands are indicated in black and 2,3-dpp bands in blue.

energy of the 2,3-dpp bridge based MLCT levels as manifested in the red shift and increase in intensity of the lowest energy absorption band (see Fig. 7). For the dceb based complexes a different situation is encountered. For **9**, the rR spectrum contains mainly dceb resonances with one extra band assigned tentatively to the 2,3-dpp ligand at 1522 cm^{-1}. For **12**, both dceb and 2,3-dpp bands are enhanced at λ_{exc} 473 nm and upon excitation at higher energy (453 and 355 nm) resonance enhancement of both dceb and 2,3-dpp bands is observed.

Photophysical properties of compounds 10–12. The photodynamics of the complexes in the 100 fs–μs time range were investigated by transient absorption (TA) and time-resolved photoluminescence (PL).

Fig. 12 shows the TA spectra of **10** and **11** at various time delays between pump and probe pulses. Both complexes show similar spectral features, demonstrating that the differences brought about by a change from chloro to iodo ligands at the Pt(II) centre are minor at sub-ns timescales, in agreement with recent reports by Rau and co-workers.[24] Across the entire probe region the spectra are dominated by a negative ground state bleach (GSB) signal, which resembles the inverted steady state absorption (indicated in grey). LMCT transitions give rise to the positive signal above 550 nm.[25,27] In the UV region a broad excited state absorptions (ESA) band centred around 375 nm is readily observed for both complexes, and assigned to absorption by the reduced ligands. It is, however, difficult to assign the excited states based on this ESA band, because the absorption of the reduced bipy and reduced 2,3-dpp ligands overlap in the UV region.[25,27,36,37] Note that in addition to the ESA signal, a strong negative GSB signal is present also in this region, resulting in a positive signal of 2 mOD only.

(A)

(B)

(C)

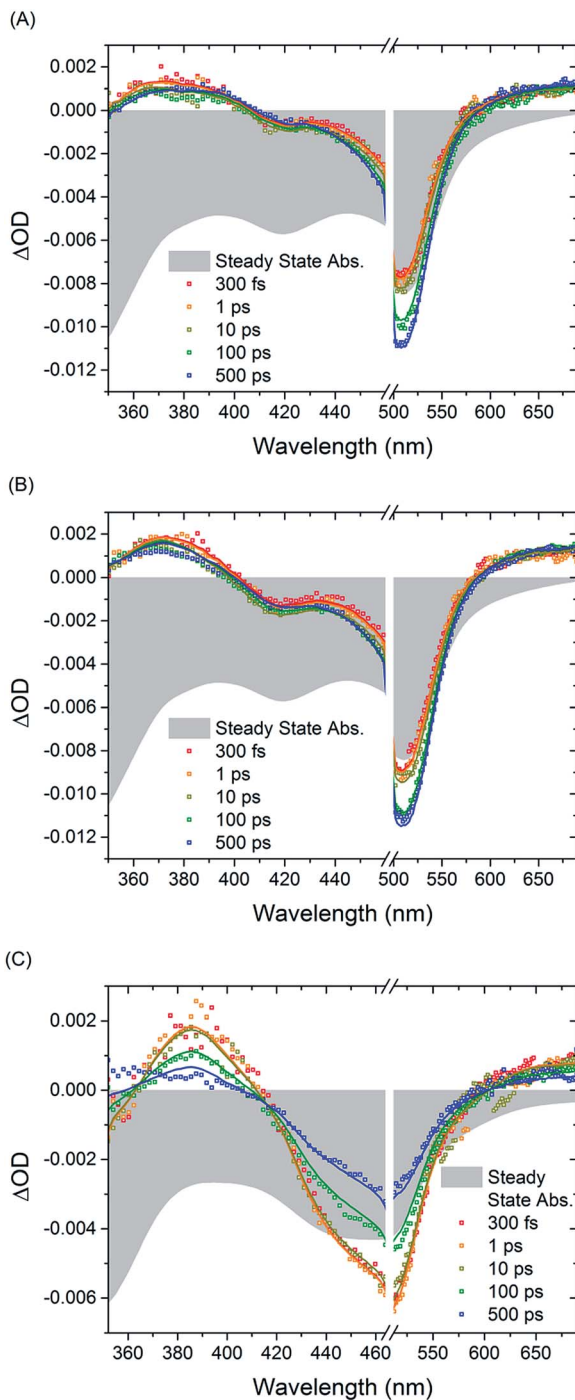**Fig. 12** Transient absorption spectra of **10** (A), **11** (B) and **12** (C) at various time delays after excitation at 480 nm (OD 0.4, 1 mm pathlength in acetonitrile) The fits obtained by singular value decomposition of the TA 2D matrix, with simultaneous fitting spectral and temporal fitting, are represented as solid curves, and the scaled and inverted steady state absorption spectrum is included as grey area.

Fig. 13 shows kinetic traces (ΔOD *vs.* time) at key wavelengths for **10** and **11**, whose photodynamical features resemble each other closely. The positive signal at 375 nm, due to intraligand transitions of the reduced ligands, is formed within the instrumental response, and only shows a minor decay over the first few ps and then remains constant up to 600 ps. The signal at 420 nm shows at least two dynamic components: a fast ~3 ps process (further increasing the negative signal amplitude) and a subsequent slower ~100 ps process decreasing the signal amplitude. Note that although the absolute signal change is less than 1 mOD, the S/N ratio at 420 nm is still sufficient to observe these two processes. Considering that the GSB signal is formed within the instrumental response time, the ~3 ps process is most likely due to decay of an overlapping ESA signal at 420 nm (or possibly vibrational cooling). The slower ~100 ps process observed at 420 nm possibly originates from either the decay of the GSB signal (*i.e.* recombination), or an increase of an overlapping ESA signal. Similarly the kinetic trace at 510 nm is mainly representative of the GSB and formed within the instrumental response time. Interestingly, a further growth of the negative signal at 510 nm is observed on a ~100 ps time scale, which is possibly due to the decrease of an overlapping ESA band. Note that a similar trend in the opposite direction is observed at 420 nm.

Detailed photophysical modelling for **10** and **11** based on target analysis is not realistic considering the overlapping ESA bands. It is, however, possible to perform a global analysis. The TA data of **10** and **11** appear to be well described by a sequential model, as illustrated by the fits included in Fig. 12 and 13. The two time constants obtained for the two compounds are close with values of 5.3 ps (3.1 ps) and 148 ps (101 ps) for **10** (**11**).

The photodynamics of **12** differ significantly from those observed for **10** and **11**. As shown in Fig. 13c, a negative GSB in the blue-green region and a ligand-based ESA band at *ca.* 390 nm are readily observed. As for **10** and **11**, the absorption bands of the reduced dceb and dpp ligands are likely to overlap. Both the ESA and GSB signals decay over ~100 ps (see Fig. 13c), indicating recombination. The GSB signal does not decay completely from −5.5 mOD to zero, but an offset of *ca.* −2.8 mOD remains. This observation illustrates the existence of excited states with distinct lifetimes (~100 ps *vs.* >1 ns), which are associated with the dceb and 2,3-dpp ligands. A time constant of 105 ps for partial recombination is obtained from a global fit of the TA data.

The very weak emission decays of **10** and **11** (Fig. 14) both show biexponential decays while for the precursors **8** and **9** single exponential decay is observed (see Table 1 and ESI,† Fig S11). The two emitting components are tentatively assigned to excited states based on the bipy and 2,3-dpp ligands and indicate that the interaction between the ligands is weak, causing potentially slow internal conversion. The emission signal of **12** is too weak to detect, due to red-shift induced by lowering of the π^* orbitals of the 2,3-dpp ligand upon coordination of Pt.

In summary, the presence of either chlorido or iodido at the catalytic (Pt) site does not significantly alter the photodynamics on the sub-ns time scales for both **10** and **11**. At least two distinct photodynamic processes are observed. The 5.3 ps (3.1 ps) process for **10** (**11**) is assigned to the decay of a ^{3}MLCT state. The 148 ps (101 ps) component for **10** (**11**) is assigned to internal conversion (*i.e.* intraligand electron transfer). Alternatively, this component may reflect relaxation to the
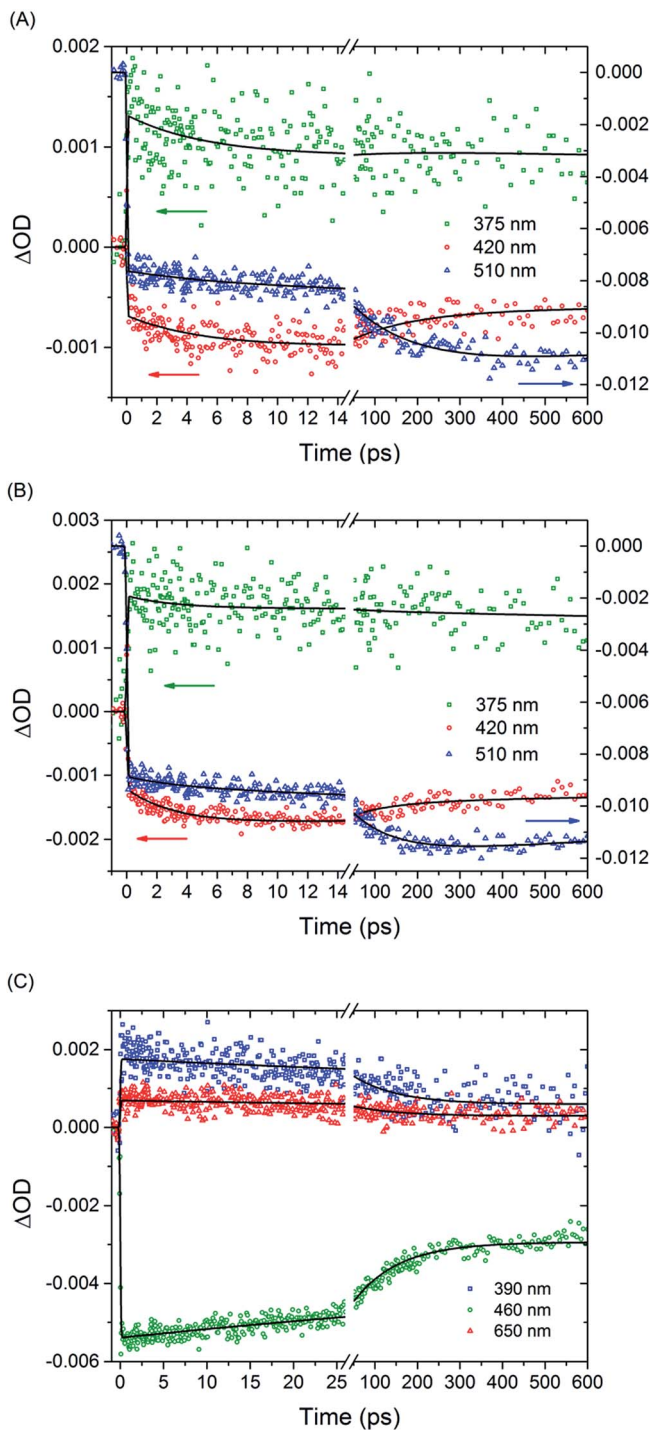
Fig. 13 Kinetic traces at representative wavelengths for **10** (A), **11** (B) and **12** (C). Excitation at 480 nm (OD 0.4, 1 mm pathlength in acetonitrile). The fits are represented as solid curves. Note the dual *y*-axis used in A and B.

(A)

$[(bpy)_2Ru(2,3dpp)PtCl_2]^{2+}$
$\tau_1 = 28$ ns (74%)
$\tau_2 = 121$ ns (26%)

(B)

$[(bpy)_2Ru(2,3dpp)PtI_2]^{2+}$
$\tau_1 = 11$ ns (64%)
$\tau_2 = 67$ ns (36%)
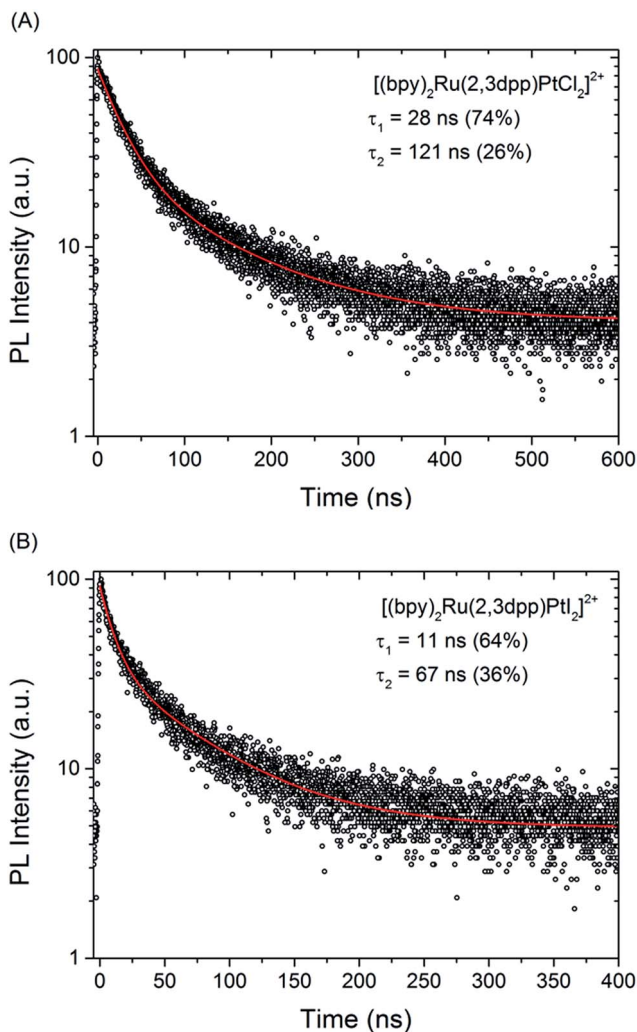
Fig. 14 Photoluminescence decays for **10** (A) and **11** (B), recorded at the emission maxima. Excitation at 462 nm (1.3 ns pulse FWHM at 1 MHz, OD 0.4, 1 cm pathlength in acetonitrile). The fits are represented as solid curves.

ground state, though this is less likely considering its absence at wavelengths with strong GSB. Some excited states are long-lived (*i.e.* >ns), as indicated by the PL decays in Fig. 14. The observation of a very weak biexponential PL decay may indicate that both bipy and 2,3-dpp based excited states are populated on the ns time scale. As for **12**, in addition to a long-lived excited state, a 105 ps partial recombination process is present, which limits the hydrogen generation efficiency of this complex.

Concluding remarks

In this contribution examples of intramolecular, *i.e.* supramolecular, photocatalytic assemblies for solar fuel generation in solution are outlined. The

discussion is limited to hydrogen generating assemblies and although intermolecular approaches have been reported extensively in the literature and in many cases shown to be effective for hydrogen generation, these have not been considered.[7–12] The aim of our studies is to identify and optimise pathways for light driven intramolecular electron transfer in multinuclear assemblies. As discussed above, optimisation of intramolecular assemblies as photocatalytic systems is extremely challenging, and in contrast to intermolecular systems, the supramolecular approach has only recently been developed. The perceived benefit of an intramolecular approach, *i.e.* a single light harvesting-catalytic assembly, is that increased photocatalytic activity can be achieved, first and foremost by overcoming limitations caused by diffusion. A key challenge faced, however, rests in communication between the active components within the supramolecular complex. The choice of bridging ligand is critical as it must allow for vectorial electron transfer from the photosensitiser to the catalytic centre (Fig. 1) but not result in rapid relaxation of excited states before reduction of the catalytic centre can take place.

The studies reported in this contribution show that controlling the MLCT levels of the bridging ligand is not the only important parameter, however. Indeed the electronic coupling between peripheral and bridging ligands is a key factor that determines to a large extent the efficiency of photoinduced electron transfer from the photosensitiser to the catalytic centre. These observations are mirrored in the photocatalytic studies that show that TONs are dependent not only on the nature of the bridging ligand, but also on the nature of the peripheral ligands. This creates additional parameters that should be considered in the optimisation of the photocatalytic behaviour of these supramolecular systems.

At present, the bimetallic supramolecular assembly approach tends to be less efficient than the intermolecular approach especially when compared to iridium based systems.[38] However, the more detailed understanding of the activity determining factors in 2 has prompted the targeted development of 3 with a nearly 40-fold increase in catalytic activity.[24] This exemplifies the rapid development possible when using a combination of spectroscopic investigation. Furthermore, when a comparison of related intra- and intermolecular Ru(II) based systems under identical conditions is made, the intramolecular approach tends to be more efficient. Importantly, the experimental conditions used in inter- and intramolecular studies tend to be different and this limits the ability to directly compare the intra- and intermolecular approaches. An important observation made by Hamm and co-workers is that for intermolecular hydrogen generation the rate determining step is not associated with electron transfer between the photosensitiser and the catalytic centre, but with hydrogen formation at the catalytic centre, which has a second order rate constant of 25 M^{-1} s^{-1}.[39] In the supramolecular systems considered in this contribution, the intramolecular electron transfer processes involving the photosensitiser/catalytic centre may not be rate limiting either. Formation of long-lived excited states that are capable of reaching the catalytic centre is, however, essential. An important aspect to consider is therefore which ligands are populated upon excitation, and the conversion between the individual excited states. A future challenge in regard to spectroscopic studies is to carry photophysical studies out under the conditions applied for catalysis and especially to deal with stability and the spectroscopic interference from byproducts of the sacrificial reductants.

Recently, considerable progress has been made in the area of intramolecular assemblies. As discussed above, the replacement of catalytic centres such as $PtCl_2$ with the iodo analogue PtI_2 leads to significantly more stable assemblies and considerably increased TONs for hydrogen generation, all without significant changes in the photophysics. Further efforts are required in this area to increase the photocatalytic efficiency by this approach, which together with detailed investigation on the electronic coupling between the peripheral and bridging ligands, can be expected to lead to a major increase in the performance of such systems for solar fuel production.

Finally, as these molecular assemblies are mainly studied in solution a sacrificial reductant is required. The need for such sacrificial agents is clearly far from ideal. Importantly, it is generally agreed that their presence is a serious limitation to the ultimate stability of the photocatalysts, irrespective of the conditions used. The first reports on the photochemical investigation of monoreduced intramolecular photocatalysts as possible intermediates in the overall catalytic cycle also open an important perspective on catalytic activity determining steps previously not accessible.[16] At present an increasing number of investigations are focusing on the immobilisation of such catalysts on solid electrode surfaces. Studies at the reduction side of water splitting include the investigation of modified NiO type sensitised photocathodes.[40] The immobilisation of the phosphonate analogue of compound **2** on NiO is also reported,[41] while TiO_2 based photoanodes for oxygen generation have been investigated separately.[42] Given the major efforts made over the last decades with dye sensitised solar cells, analogous approaches with photocatalysis are likely to see much more rapid progress given the experience already developed.

Experimental part

Synthetic procedures

[Ru(bpy)$_2$(2,3-dpp)](PF$_6$)$_2$·3H$_2$O. *cis*-[Ru(bipy)$_2$Cl$_2$] (142 mg, 0.27 mmol) dissolved in 10 cm^3 of ethanol was added drop-wise to a solution of 2,3-dpp (126 mg, 0.54 mmol) in 10 ml of ethanol–water (3 : 1) over 5 h. The reaction mixture was heated at reflux for 24 h. Subsequently the mixture was allowed to cool to room temperature and the ethanol was removed *in vacuo*. To remove an excess of ligand the residue was dissolved in 10 ml of water and filtered. The filtrate was precipitated in an aqueous solution of NH_4PF_6 followed by filtration. The product was then washed with H_2O and Et_2O. As the attempt to recrystallise from acetone–toluene failed, recrystallisation was carried out from acetone–water (3 : 1) and afforded a red solid. Yield: 45% (121 mg, 0.122 mmol). ^{1}H NMR (400 MHz, acetone) δ[ppm] = 8.84 (dd, J = 13.1, 5.4 Hz, 4H, H-a), 8.67 (ddd, J = 4.8, 1.7, 0.9 Hz, 1H, H-6′), 8.62 (d, J = 3.1 Hz, 1H, H-5), 8.34–8.29 (d, J = 5.9 Hz,1H, H-d), 8.29–8.21 (m, 5H, H-6, 4*H-b), 8.19 (dd, J = 7.7, 1.7 Hz, 1H, H-3′), 8.12–8.10 (m, 1H, H-4′), 8.10–8.07 (m, 2H, H-3″, H-d), 8.05 (d, J = 5.9 Hz, 2H, 2*H-d), 7.84 (ddd, J = 8.4, 7.7, 1.5 Hz, 1H, H-5″), 7.71–7.64 (m, 2H, H-5′, H-c), 7.64–7.57 (m, 3H, 3*H-c), 7.51–7.46 (m, 1H, H-4″), 7.43 (d, J = 7.9 Hz, 1H, H-6″). CHN analysis: calc. C = 41.18%, H = 3.25%, N = 11.30%. Found: C = 41.60%, H = 2.50%, N = 10.93%. MS (ESI in CH_3CN): m/z = 793.3 ([M–PF$_6$]$^+$), 324.2 ([M–2PF$_6$]$^{2+}$).

[Ru(bpy)$_2$(2,3-dpp)PtCI$_2$](PF$_6$)$_2$·3H$_2$O. [Pt(dmso)$_2$Cl$_2$] (107 mg, 0.254 mmol) was dissolved in 5 cm^3 of CH_2Cl_2 and Ru(bipy)$_2$(2,3-dpp)](PF$_6$)$_2$·3H$_2$O (161 mg,

0.162 mmol) dissolved in 6 cm^3 of CH$_2$Cl$_2$ was added drop-wise to the solution over 1 h. The mixture was heated at reflux for 24 h and subsequently allowed to cool to room temperature. The solution was precipitated in *n*-hexane followed by filtration. The product was then washed with *n*-hexane, H$_2$O and Et$_2$O. Recrystallisation from acetone–water (3 : 1) afforded a purple solid. Yield: 92% (188 mg, 0.149 mmol). ^{1}H NMR (400 MHz, acetone) δ[ppm] = 9.66–9.54 (m, 1H, H-6′), 9.45 and 9.41 (d, J = 3.8, 5.5 Hz, 1H, H-5), 9.22 and 9.15 (d, J = 7.2, 8.1 Hz, 1H), 9.08–8.73 (m, 6H), 8.72–8.44 (m, 2H), 8.39–8.19 (m, 5H), 8.16–7.45 (m, 10H). CHN analysis: calc. C = 32.47%, H = 2.56%, N = 8.91%. Found: C = 32.85%, H = 2.08%, N = 8.24%. MS (ESI in CH$_3$CN): m/z = 1059.0 ([M–PF$_6$]$^+$), 456.7 ([M–2PF$_6$]$^{2+}$), 326.0 ([M–2PF$_6$–2PtCl$_2$]$^{2+}$).

[Ru(bipy)$_2$(2,3-dpp)PtI$_2$](PF$_6$)$_2$·2H$_2$O. [Pt(dmso)$_2$I$_2$] (100 mg, 0.165 mmol) was dissolved in 40 cm^3 of EtOH and [Ru(bipy)$_2$(2,3-dpp)]$^{2+}$ (120.0 mg, 0.121 mmol) dissolved in 25 cm^3 of acetone/EtOH (4 : 1) was added drop-wise to the solution over 1 h. The mixture was heated at reflux for 24 h and subsequently allowed to cool to room temperature. The acetone was removed *in vacuo* and the solution was precipitated in an aqueous solution of NH$_4$PF$_6$ followed by filtration. The product was then washed with EtOH (2 cm^3), H$_2$O and Et$_2$O. Recrystallisation from acetone–acetonitrile (1 : 1) afforded a purple solid. Yield: 71% (122 mg, 0.086 mmol). ^{1}H NMR (400 MHz, acetone) δ[ppm] = 10.23 and 10.20 (2*d, J = 5.4 Hz, 1H, H-6′), 9.99 and 9.89 (2*d, J = 3.9, 4.0 Hz, 1H, H-5), 9.21 and 9.12 (d, J = 8.9, 8.1 Hz, 1H), 9.06–8.54 (m, 7H), 8.66 and 8.49 (d, J = 3.9, 3.6 Hz, 1H, H-6), 8.39–8.23 (m, 5H), 8.19 (d, J = 5.6 Hz, 1H), 8.16–7.95 (m, 4H), 7.81 and 7.75 (t, J = 7.0, 6.6 Hz, 1H), 7.70–7.48 (m, 4H) CHN analysis: calc. C = 28.71%, H = 2.13%, N = 7.88%. Found: C = 28.90%, H = 1.80%, N = 7.59%. MS (ESI in CH$_3$CN): m/z = 1241.1 ([M–PF$_6$]$^+$), 548.7 ([M–2PF$_6$]$^{2+}$).

[Ru(dceb)$_2$(2,3-dpp)](PF$_6$)$_2$. *cis*-[Ru(dceb)$_2$Cl$_2$] (403 mg, 0.521 mmol) dissolved in 10 cm^3 of ethanol was added drop-wise to a solution of 2,3-dpp (211 mg, 0.900 mmol) in 10 cm^3 of ethanol–water (3 : 1) over 3 hours. The reaction mixture was heated at reflux for 24 h. Subsequently the mixture was allowed to cool to room temperature and the ethanol was removed *in vacuo*. To remove an excess of ligand the residue was dissolved in 100 ml of water and filtered. The filtrate was precipitated in an aqueous solution of NH$_4$PF$_6$ followed by filtration. The product was then washed with H$_2$O and Et$_2$O. Recrystallisation from acetone–water (3 : 1) afforded a dark red/purple solid. Yield: 49% (314 mg, 0.256 mmol). ^{1}H NMR (400 MHz, acetone) δ[ppm] = δ 9.42–9.33 (m, 4H, 4*Ha), 8.69 (d, J = 4.8 Hz, 1H, H6′), 8.66 (d, J = 3.0 Hz, 1H, H5), 8.62 (d, J = 5.8 Hz, 1H, Hd), 8.41–8.34 (m, 3H, Hd), 8.32 (d, J = 3.1 Hz, 1H, H6), 8.20 (td, J = 7.7, 1.7 Hz, 1H, H4′), 8.16–8.10 (m, 3H, H3″, H3′, Hc), 8.03 (dd, J = 5.8, 1.6 Hz, 1H, Hc), 7.96 (m, 2H, 2*Hc), 7.91 (td, J = 8.3, 1.4 Hz, 1H, H5″), 7.70 (m, 1H, H5′), 7.52–7.49 (m, 1H, H4″), 7.46 (d, J = 8.4 Hz, 1H, H6″), 4.53–4.42 (m, 8H, O–CH$_2$), 1.42–1.35 (m, 12H, O–CH$_2$–CH$_3$). Elemental analysis: calc. C = 45.07%, H = 3.45%, N = 9.14%. Found: C = 44.57%, H = 3.22%, N = 9.03%. MS (ESI in CH$_3$CN): m/z = 1081.4 ([M–PF$_6$]$^+$), 468.4 ([M–2PF$_6$]$^{2+}$).

[Ru(dceb)$_2$(2,3-dpp)PtCl$_2$](PF$_6$)$_2$·2H$_2$O. [Pt(dmso)$_2$Cl$_2$] (59 mg, 0.140 mmol) was dissolved in 5 cm^3 of CH$_2$Cl$_2$ and [Ru(dceb)$_2$(2,3-dpp)]$^{2+}$ (112.7 mg, 0.092 mmol) dissolved in 6 ml of CH$_2$Cl$_2$ was added drop-wise to the solution over 1 h. The mixture was heated at reflux for 29 h and then allowed to cool to room temperature. The solution was precipitated in *n*-hexane followed by filtration. The

product was then washed with H_2O and Et_2O. Recrystallisation from acetone–water (2 : 1) afforded a red solid. Yield: 85% (119.4 mg, 0.078 mmol). ^{1}H NMR (400 MHz, acetone) δ[ppm] = 9.57–8.77 (m, 9H), 8.50–7.50 (m, 13H), 4.59–4.34 (m, 8H, O–CH_2), 1.46–1.30 (m, 12H, O–CH_2–CH_3). Elemental analysis: calc. C = 36.16%, H = 3.03%, N = 7.33%. Found: C = 36.10%, H = 2.52%, N = 7.17%.

[Ru(dceb)$_2$(2,3-dpp)PtI$_2$](PF$_6$)$_2$·4H$_2$O. [Pt(dmso)$_2$I$_2$] (44.6 mg, 0.074 mmol) was dissolved in 5 ml of CH_2Cl_2 and [Ru(dceb)$_2$(2,3-dpp)]$^{2+}$ (75 mg, 0.061 mmol) dissolved in 6 ml of CH_2Cl_2 was added drop-wise to the solution over 1 h. The mixture was heated at reflux for 25 h and then allowed to cool to room temperature. The solution was precipitated in *n*-hexane followed by filtration. The red product was then washed with H_2O and Et_2O. Yield: 85% (90.6 mg, 0.052 mmol). ^{1}H NMR (400 MHz, acetone) δ[ppm] = 10.23 and 10.19 (2*d, J = 6.2, 5.4 Hz 1H, H-6′), 10.03 and 9.94 (2*d, J = 3.9, 3.6 Hz, 1H, H-5), 9.49–9.39 (m, 2H), 9.38–8.45 (m, 6H), 8.46–7.89 (m, 10H), 7.84–7.76 (m, 1H), 7.60 (t, J = 6.9 Hz, 1H), 4.54–4.40 (m, 8H, O–CH_2), 1.47–1.30 (m, 12H, O–CH_2–CH_3). Elemental analysis: calc. C = 31.63%, H = 2.89%, N = 6.41%. Found: C = 30.73%, H = 2.08%, N = 6.38% MS (ESI in CH_3CN): m/z = 1531.2 ([M–PF$_6$]$^+$), 692.5 ([M–2PF$_6$]$^{2+}$), 468.4 ([M–2PF$_6$–2PtCI$_2$]$^{2+}$).

Instrumentation and procedures

^{1}H-NMR spectra were obtained on a Bruker Advance 400 NMR spectrometer in deuterated solvents (acetone-d$_6$, acetonitrile-d$_3$, dmso-d$_6$) with either TMS (tetramethylsilane) or residual solvent peaks as reference. Free induction decays (FID) were processed using MestReNova. Coupling is indicated using the abbreviations: s (singlet), d (doublet), t (triplet), q (quartet), dd (doublet of a doublet), m (multiplet). The coupling constants J are reported in Hz. UV/vis absorption spectra were recorded on an Agilent Technologies 8453 photodiode array spectrometer using a 1 cm path length quartz cell. Emission spectra (±5 nm) were obtained using a LS50B luminescence spectrophotometer, equipped with a red sensitive Hamamatsu R928 PMT detector, interfaced with an Elonex PC466 employing Perkin-Elmer FL WinLab custom built software, with the same optical density (OD ≈ 0.2) at λ_{exc}. Both absorption and emission spectra were recorded at room temperature. Raman spectra were recorded at 473 nm, 457 nm and 355 nm (Cobolt Lasers 50 mW) in 1 cm path length quartz cuvettes. The excitation beam was focused at the sample using a 10 cm focal length parabolic mirror at *ca.* 35° with respect to the collection axis. Raman scattering was collected and collimated with a 2.5 cm diameter, 15 mm focal length plano-convex mirror, filtered to remove Rayleigh scattering using a Steep Edge long pass filter (Semrock), focused into the spectrograph (Shamrock 303, Andor Technology, 1200 l mm^{-1} grating blazed at 500 nm), and imaged onto an iDus-420-BEX2-DD CCD camera (Andor Technology). ESI-MS spectra in acetonitrile were recorded in positive mode on a Triple Quadrupole LC/MS/MS mass spectrometer (API 3000, Perkin-Elmer Sciex Instruments). CHN analyses were carried out using Exador Analytical CE440 by the Microanalytical Department, University College Dublin, Ireland. The femtosecond transient absorption (TA) setup used was described earlier. The instrument response time was estimated to be ~120 fs in the blue region and ~250 fs at 350 nm, based on the coherent artefact signal from the solvent alone.[25] For TA experiments the compounds were dissolved in anhydrous acetonitrile (Sigma-

Aldrich, purity > 99.9%) with 0.4 OD at 480 nm (excitation wavelength) in a 1 mm path length quartz cuvette. The TA data were numerically corrected for chirp, and analysed using the Glotaran program.[43] Time-resolved photoluminescence experiments were performed using a FluoroMax Spectrofluorometer extended for time-correlated single photon counting (TCSPC) (HORIBA JOBIN YVON, FluoroMax-4 TCSPC). A NanoLED-460 laser (462 nm, 1.3 ns pulse duration) was used for excitation. **10** and **11** were excited at a repetition rate of 1 MHz. Samples were dissolved in acetonitrile and degassed using dry N_2 gas before the measurement.

Experimental conditions for photocatalytic experiments

In advance of the photocatalytic experiments all solutions used were degassed. A stock solution with a known sample weight was dissolved in 20 ml of acetonitrile. Solutions of the complexes were prepared in the GC vials by mixing 1.2 ml of the stock solution, 0.2 ml of H_2O (10%) and 0.6 ml of triethylamine under a nitrogen atmosphere. The solutions were 0.12 mM in complex. The solutions were irradiated for 470 nm (LED, 40–50 mW) from beneath with forced air cooling to keep the reaction mixtures at room temperature. After irradiation the hydrogen gas evolved was determined by headspace GC (Bruker Scion) after 0, 1, 2, 4, 6, 18 and 24 h and TON and TOF values were determined in triplicate. A thermal conductivity detector (column: Mol. Sieve 5Å 75 m × 0.53 mm I.D., oven temp. 70 °C, flow rate 22.5 ml min^{-1}, detector temp. 200 °C) with argon as carrier gas was used.

Acknowledgements

Notes and references

1 V. Balzani, A. Credi and M. Venturi, *ChemSusChem*, 2008, **1**, 26.

2 *Annual Energy Outlook 2011-With Projections to 2033*, U.S. Energy Information Administration, U.S. Department of Energy, DOE/EIA, Washington, DC, 20585, 2011.

3 N. S. Lewis and D. G. Nocera, *Proc. Natl. Acad. Sci. U. S. A.*, 2006, **103**, 15729.

4 A. Hagfeldt and M. Grätzel, *Acc. Chem. Res.*, 2000, **33**, 269.

5 L. Sun, L. Hammarström, B. Åkermark and S. Styring, *Chem. Soc. Rev.*, 2001, **30**, 36.

6 (*a*) E. Fujita, *Coord. Chem. Rev.*, 1999, **185**, 373; (*b*) A. J. Morris, G. J. Meyer and E. Fujita, *Acc. Chem. Res.*, 2009, **42**, 1983; (*c*) W. T. Eckenhoff and R. Eisenberg, *Dalton Trans.*, 2012, 13004; (*d*) S. Losse, J. G. Vos and S. Rau, *Coord. Chem. Rev.*, 2010, **254**, 2492.

7 (*a*) K. Sakai and H. Ozawa, *Coord. Chem. Rev.*, 2007, **251**, 2753; (*b*) A. Inagaki and M. Akita, *Coord. Chem. Rev.*, 2010, **254**, 1220; (*c*) M. Schulz, M. Karnahl, M. Schwalbe and J. G. Vos, *Coord. Chem. Rev.*, 2012, **256**, 1682; (*d*) P. D. Frischmann, K. Mahata and F. Wurther, *Chem. Soc. Rev.*, 2013, **42**, 1847; (*e*) S. Rau, D. Walther and J. G. Vos, *Dalton Trans.*, 2007, 915; (*f*) G. F. Manbeck and K. J. Brewer, *Coord. Chem. Rev.*, 2013, **257**, 1660; (*g*) Y. Halpin, M. T. Pryce, S. Rau, D. Dini and J. G. Vos, *Dalton Trans.*, 2013, 16243.

8 H. Ozawa and K. Sakai, *Chem. Commun.*, 2011, **47**, 2227.

9 V. Artero, M. Chavarot-Kerlidou and M. Fontecave, *Angew. Chem., Int. Ed.*, 2011, **50**, 7238.

10 (*a*) M. Karnahl, C. Kuhnt, F. W. Heinemann, M. Schmitt, S. Rau, J. Popp and B. Dietzek, *Chem. Phys.*, 2012, **393**, 65; (*b*) K. Peuntinger, T. D. Pilz, R. Staehle, M. Schaub, S. Kaufhold, L. Petermann, M. Wunderlin, H. Goerls, F. W. Heinemann, J. Li, T. Drewello, J. G. Vos, D. M. Guldi and S. Rau, *Dalton Trans.*, 2014, 13683; (*c*) M. Karnahl, C. Kuhnt, F. Ma, A. Yartsev, M. Schmitt, B. Dietzek, S. Rau and J. Popp, *ChemPhysChem*, 2011, **12**, 2101; (*d*) M. G. Pfeffer, B. Schäfer, G. Smolentsev, J. Uhlig, E. Nazarenko, J. Guthmuller, C. Kuhnt, M. Wächtler, B. Dietzek, V. Sundström and S. Rau, *Angew. Chem., Int. Ed.*, 2015, **54**, 5044; (*e*) M. Schwalbe, M. Karnahl, H. Gorls, D. Chartrand, F. Laverdiere, G. S. Hanan, S. Tschierlei, B. Dietzek, M. Schmitt, J. Popp, J. G. Vos and S. Rau, *Dalton Trans.*, 2009, 4012.

11 (*a*) J. D. Knoll, S. M. Arachchige and K. J. Brewer, *ChemSusChem*, 2011, **4**, 252; (*b*) J. D. Knoll, S. M. Arachchige, G. Wang, K. Rangan, R. Miao, S. L. H. Higgins, B. Okyere, M. Zhao, P. Croasdale, K. Magruder, B. Sinclair, C. Wall and K. J. Brewer, *Inorg. Chem.*, 2011, **50**, 8850; (*c*) J. D. Knoll, S. L. H. Higgins, T. A. White and K. J. Brewer, *Inorg. Chem.*, 2013, **52**, 9749.

12 P. Lei, M. Hedlund, R. Lomoth, H. Rensmo, O. Johansson and L. Hammarström, *J. Am. Chem. Soc.*, 2008, **130**, 26.

13 S. Rau, B. Schäfer, D. Gleich, E. Anders, M. Rudolph, M. Friedrich, H. Görls, W. Henry and J. G. Vos, *Angew. Chem., Int. Ed.*, 2006, **45**, 6215.

14 M. Karnahl, C. Kuhnt, F. Ma, A. Yartsev, M. Schmitt, B. Dietzek and S. Rau, *ChemPhysChem*, 2011, **12**, 2101.

15 S. Tschierlei, M. Karnahl, M. Presselt, B. Dietzek, J. Guthmüller, L. Gonzalez, M. Schmitt, S. Rau and J. Popp, *Angew. Chem., Int. Ed.*, 2010, **49**, 3981.

16 L. Zedler, J. Guthmuller, I. Rabelo de Moraes, S. Kupfer, S. Krieck, M. Schmitt, J. Popp, S. Rau and B. Dietzek, *Chem. Commun.*, 2014, **50**, 5227.

17 Y. Takami, K. Watanabe, K. Koike, H. Inoue, T. Morimoto and O. Ishitani, *Faraday Discuss.*, 2012, **155**, 115.

18 G. Singh Bindra, M. Schulz, A. Paul, R. Groarke, S. Soman, J. L. Inglis, W. R. Browne, M. Pfeffer, S. Rau, B. J. MacLean, M. T. Pryce and J. G. Vos, *Dalton Trans.*, 2012, 13050.

19 G. Singh Bindra, M. Schulz, A. Paul, S. Soman, R. Groarke, J. Inglis, M. T. Pryce, W. R. Browne, S. Rau, B. J. Maclean and J. G. Vos, *Dalton Trans.*, 2011, 10812.

20 H. Ozawa, Y. Yokoyama, M. Haga and K. Sakai, *Dalton Trans.*, 2007, 1197.

21 S. Soman, G. Singh Bindra, A. Paul, R. Groarke, J. C. Manton, F. M. Connaughton, M. Schulz, D. Dini, C. Long, M. T. Pryce and J. G. Vos, *Dalton Trans.*, 2012, 12678.

22 S. Tschierlei, M. Presselt, C. Kuhnt, A. Yartsev, T. Pascher, V. Sundström, M. Karnahl, M. Schwalbe, B. Schäfer, S. Rau, M. Schmitt, B. Dietzek and J. Popp, *Chem.–Eur. J.*, 2009, **15**, 7678.

23 M. G. Pfeffer, B. Schäfer, C. Kuhnt, M. Schmitt, J. Popp, J. Guthmuller, G. Smolentsev, J. Uhlig, E. Nazarenko, V. Sundström, L. González, B. Dietzek and S. Rau, *Angew. Chem.*, 2015, **54**, 5044.

24 M. G. Pfeffer, T. Kowacs, M. Wächtler, J. Guthmuller, B. Dietzek, J. G. Vos and S. Rau, *Angew. Chem., Int. Ed. Engl.*, 2015, **54**, 6627.

25 Q. Pan, F. Mecozzi, J. P. Korterik, D. Sharma, J. L. Herek, J. G. Vos, W. R. Browne and A. Huijser, *J. Phys. Chem. C*, 2014, **118**, 20799.

26 A. Cannizzo, F. van Mourik, W. Gawelda, G. Zgrablic, C. Bressler and M. Chergui, *Angew. Chem., Int. Ed.*, 2006, **45**, 3174.

27 S. Wallin, J. Davidsson, J. Modin and L. Hammarström, *J. Phys. Chem. A*, 2005, **109**, 4697.

28 N. H. Damrauer, G. Cerullo, A. Yeh, T. R. Boussie, C. V. Shank and J. K. McCusker, *Science*, 1997, **275**, 54.

29 (*a*) S. Wallin, J. Davidsson, J. Modin and L. Hammarström, *J. Phys. Chem. A*, 2005, **109**, 4697; (*b*) M. Krejcik and A. A. Vlcek, *J. Electroanal. Chem.*, 1991, **313**, 243.

30 (*a*) J. T. Hewitt, J. J. Concepcion and N. H. Damrauer, *J. Am. Chem. Soc.*, 2013, **135**, 12500; (*b*) J. T. Hewitt, P. J. Vallett and N. H. Damrauer, *J. Phys. Chem. A*, 2012, **116**, 11536.

31 This value was obtained from analysis of the data shown in Fig. 9 by modelling of the species associated spectra (SAS) shape. The unit of SAS is OD which takes into account potential differences in oscillator strength.

32 G. Denti, S. Campagna, L. Sabatino, S. Serroni, M. Ciano and V. Balzani, *Inorg. Chem.*, 1990, **29**, 4150.

33 J. Hirschmann, G. Singh Bindra, S. Soman, A. Paul, R. Groarke, M. Schulz, M. T. Pryce, W. R. Browne, S. Rau and J. G. Vos, *Dalton Trans.*, 2011, 10545.

34 W. R. Browne, N. M. O'Boyle, W. Henry, S. Horn, A. L. Guckian, T. Fett, C. M. O'Connor, M. Duati, L. De Cola, C. G. Coates, K. L. Ronayne, J. J. McGarvey and J. G. Vos, *J. Am. Chem. Soc.*, 2005, **127**, 1229.

35 (*a*) K. Maruszewski, K. Bajdor, D. P. Strommen and J. R. Kincaid, *J. Phys. Chem.*, 1995, **99**, 6286; (*b*) P. Mallick, G. D. Danzer, D. P. Strommen and J. R. Kincaid, *J. Phys. Chem.*, 1988, **92**, 5628.

36 M. Krejčík and A. A. Viček, *J. Electroanal. Chem.*, 1991, **313**, 243.

37 R. M. Berger, *Inorg. Chem.*, 1990, **29**, 1920.

38 (*a*) L. L. Tinker, N. D. McDaniel, P. N. Curtin, C. K. Smith, M. J. Ireland and S. Bernhard, *Chem.–Eur. J.*, 2007, **13**, 8726; (*b*) P. N. Curtin, L. L. Tinker, C. M. Burgess, E. D. Cline and S. Bernhard, *Inorg. Chem.*, 2009, **48**, 10498.

39 B. Probst, A. Rodenberg, M. Guttentag, P. Hamm and R. Alberto, *Inorg. Chem.*, 2010, **49**, 6453.

40 (*a*) L. Li, L. Duan, F. fen, C. Li, M. Wang, A. Hagfeldt, L. Sun and L. Hammarstrom, *Chem. Commun.*, 2012, **48**, 988; (*b*) Z. Li, M. He, Z. Huang, U. Ozkan and Y. Wu, *J. Am. Chem. Soc.*, 2013, **135**, 11696; (*c*) F. Odobel and Y. Pellegrin, *J. Phys. Chem. Lett.*, 2013, **4**, 2551.

41 M. Braumüller, M. Schulz, D. Sorsche, M. Pfeffer, M. Schaub, J. Popp, B.-W. Park, A. Hagfeldt, B. Dietzek and S. Rau, *Dalton Trans.*, 2015, 5577.

42 (*a*) J. R. Swierk and T. E. Mallouk, *Chem. Soc. Rev.*, 2013, **42**, 2357; (*b*) L. Alibabaei, M. K. Brennaman, M. R. Norris, B. Kalanyan, W. Song, M. D. Losego, J. J. Conception, R. A. Binstead, G. N. Parsons and T. J. Meyer, *Proc. Natl. Acad. Sci. U. S. A.*, 2013, **110**, 20008; (*c*) Y. Gao, X. Ding, J. Liu, L. Wang, Z. Lu, L. Li and L. Sun, *J. Am. Chem. Soc.*, 2013, **135**, 4219.

43 J. J. Snellenburg, S. P. Laptenok, R. Seger, K. M. Mullen and I. H. M. van Stokkum, *J. Stat. Software*, 2012, **49**, 1–22.